

Analyzing Different Parameterization Methods in GNSS Tomography Using the COST Benchmark Dataset

Zohreh Adavi , Witold Rohm , and Robert Weber

Abstract—GNSS tomography is an emerging remote sensing technique in the field of meteorology that is gaining increased attention in recent years. This method is used as a tool for atmospheric (particularly tropospheric) sensing and then applied in nowcasting and forecasting research. The tomographic approach can be used to determine the distribution of water vapor (WV), the most active component of the atmosphere. WV is one of the most important drivers of convection and precipitation. In this method, numerous line-of-sight integral observations at different locations and directions are used to derive a 3-D distribution of a WV structure. One of the challenges in GNSS tomography is that different parameterization methods are used for computing the design matrix. Here, the effect of the straight-line method versus the ray-tracing method is investigated for computing the length of a ray which passes through the model element. In addition, the effect of considering the topography of the area in the tomography model is analyzed. The accuracy of the developed model is verified using radiosonde measurements in the COST benchmark dataset. Results show that the Eikonal ray-tracing method is superior to other schemes whether used with topography or not. The mean values of RMSE of estimated wet refractivity with respect to the radiosonde profiles for these schemes are about 1.313 and 1.766 ppm, respectively. This work is conducted within COST Action ES1206 on “Advanced global navigation satellite systems tropospheric products for monitoring severe weather events and climate (GNSS4SWEC) (2013–2017)” and IAG Working Group “GNSS tomography.”

Index Terms—Global navigation satellite systems (GNSS), ray-tracing, tomography, topography.

I. INTRODUCTION

DESPITE its small contribution to the volume of the Earth’s atmosphere, water vapor (WV) plays a significant role in the formation of clouds, rain, and snow; air pollution; and acid rain [1], [2]. Hence, improved WV monitoring results in more accurate predictions of precipitation and severe weather conditions, and it helps to ameliorate the understanding of climate change by meteorologists [3]–[7].

Manuscript received December 10, 2019; revised April 8, 2020, July 1, 2020, July 23, 2020, and September 24, 2020; accepted September 25, 2020. Date of publication September 30, 2020; date of current version October 19, 2020. This work was supported within International Academic Partnership Programme by Polish National Agency for Academic Exchange (NAWA) under Contract PPI/APM/2018/1/00013/U/00. (Corresponding author: Zohreh Adavi.)

Zohreh Adavi and Robert Weber are with TU Wien, 1040 Vienna, Austria (e-mail: zohreh.adavi@ge.tuwien.ac.at; robert.weber@tuwien.ac.at).

Witold Rohm is with the Wrocław University of Environmental and Life Sciences, 50-375 Wrocław, Poland (e-mail: witold.rohm@upwr.edu.pl).

Digital Object Identifier 10.1109/JSTARS.2020.3027909

Various techniques like lidar [8]–[10], radiosonde, WV radiometer [11], [12], and ground sensors [1], [4], [13] have been used to measure the spatiotemporal variations of this parameter. However, these methods have limitations such as high unit costs and low spatiotemporal resolution. Instead, the determination of WV using the global navigation satellite systems (GNSS) is a low cost and effective technique with reasonable precision and more spatiotemporal resolution than was provided by the previous techniques. Over the past two decades, the potential of using GNSS to determine the 4-D wet refractivity and WV fields using tomography has been evaluated in various studies [14]–[26].

GNSS tomography is an all-weather condition remote sensing technique that can be used to reconstruct the WV or the wet refractivity in the Earth’s atmosphere. In this method, the atmosphere is modeled through a finite number of 3-D elements (voxels). As recent studies show, the tomography solution [16] is very sensitive to the *a priori* data and much less dependent on the number of observations used in a single epoch. One of the clear limitations of a few models (e.g., TOMO2) tested by Brenot *et al.* [16] was a simplification of the parameterization: the signal path was parameterized as a straight line and no topography model has been considered. Therefore, the signal path in the model is, on average, shorter than in reality, which introduces biases [27]. Moreover, a lack of topography modeling results in an unrealistically high value of refractivity, especially over rough topography. One of the solutions is to use a precise ray-tracing method to account for the bending effects.

In recent years, different ray-tracing methods have been developed in the GNSS or VLBI community to calculate different parameters such as slant tropospheric delay (STD) [28]–[30]. In the GNSS tomography field, pioneering research by Aghajany and Amerian [31] applied 2-D and 3-D Eikonal ray-tracing methods in WV tomography with initial testing of its impact on the reconstructed field. Möller and Landskron [27] developed a mixed linear ray-tracing method to reconstruct the bent path which can be used for near-real-time applications. However, in these studies, the effect of the different coordinates types used in the straight-line strategy compared to the ray-tracing method was not investigated. In addition, the impact of the topography of the area of interest to design a tomography model was not evaluated.

Therefore, in this article, we have analyzed the effect of a straight-line (in ENU and UTM coordinate systems) ray-tracing

method versus a 2-D Eikonal method. In addition, the effect of the topography of the area in tomographic modeling was studied. As a fact, tomography quality is a complex function of geometry (observations distribution, model resolution, time interval), inversion, regularization algorithms, and initial conditions used in the model [16]. Hence, all the research efforts that try to establish an understanding of these complex problems are of interest to the GNSS tomography community. Section II discusses the tomographic reconstruction of the wet refractivity parameters. In that section, straight-line geometry, the Eikonal ray-tracing method, and voxel design using the topography effect are described. Section III introduces the study area. The numerical results are discussed in Section IV. In that section, the topography impact on the tomography modeling using different ray-tracing schemes is compared to radiosonde data in the COST benchmark dataset. Finally, Section V presents conclusions.

II. METHODOLOGY

In this section, the tomographic reconstruction problem of wet refractivity is introduced. Then, the Eikonal ray-tracing method and straight-line geometry utilized for populating the design matrix are described. Finally, the voxel design for accounting for the topography effect is defined.

A. Tomographic Modeling

The spatiotemporal structure of tropospheric wet refractivity (\mathbf{N}_w) can be reconstructed using the GNSS tomography technique. In this method, the troposphere is discretized into a number of elements. Then, using the GNSS signals, which cross voxels, the spatial and temporal behaviors of the wet refractivity field in this part of the atmosphere were estimated. This kind of inversion problem is formulated by the following equation:

$$\mathbf{SWD} = \mathbf{A} \mathbf{N}_w \quad (1)$$

where \mathbf{SWD} is the vector of the slant wet delays and \mathbf{N}_w is the vector of unknown parameters containing the wet refractivity of each element. The wet refractivity is measured in [mm/km], and it is normally a unit-less quantity. \mathbf{A} is the design matrix that links the observation space to the space of unknowns. The dimensions of \mathbf{A} are $m \times n$ where m is the number of measurements and n is the number of voxels. The parameter m depends on the selected time resolution, the number of GPS stations, and the number of visible satellites. The general form of this matrix is as follows [23]:

$$\mathbf{A} = \begin{bmatrix} d_{11} & 0 & 0 & 0 & \dots & d_{1n} \\ d_{21} & d_{22} & d_{23} & 0 & \dots & d_{2n} \\ \vdots & \vdots & \vdots & \vdots & \ddots & \vdots \\ d_{m1} & d_{m2} & 0 & d_{m4} & \dots & d_{mn} \end{bmatrix}. \quad (2)$$

In this equation d_{ij} is the length of the i th ray, which passes through the j th voxel. The structure matrix \mathbf{A} depends on the geometry of the model (size of voxels) as well as the geometry of the measurements [15]. Therefore, the system of observation equations is a mixed-determined, because the model elements are either over- or under-determined during the time span within

TABLE I
APPLIED DATA SET AND TIME PERIOD IN TOMOGRAPHY MODELING

GNSS Network	Numerical Weather Model	RS Locations in geodetic system	Time Period
72 GNSS Stations	ALADIN-CZ	10548 Lat: 50.57° Lon: 10.38° H _{st} : 497 m	DoYs 160–176 in 2013
Average distance: 48km Height: 70m–885m	Horizontal resolution: 4.7km × 4.7km Vertical resolution: 87 model levels Time of analysis: 00, 06, 12, 18	10771 Lat: 49.43° Lon: 11.90° H _{st} : 465 m	

the area of interest [32]. Because of the limited number of simultaneously visible satellites and the continuous changes of the atmosphere, the tropospheric reconstruction problem is not well constrained and the reconstruction quality is highly time-dependent [33], [34]. In consequence, extra constraints and the regularization method should be used to solve the ill-posed (1). Here, horizontal and vertical constraints were added. The reader is referred to Adavi and Weber [35] for more details. Moreover, the Landweber regularization algorithm was applied to reconstruct the wet refractivity field. This technique belongs to the family of iterative regularization schemes. Therefore, based on this method, (1) is solved as follows [14], [35]:

$$\mathbf{N}_w^{k+1} = \mathbf{N}_w^k + \lambda_k \mathbf{A}^T (\mathbf{SWD} - \mathbf{A} \mathbf{N}_w^k) \quad (3)$$

whereby λ_k and k are the relaxation parameter and the iteration number, respectively [36], [37]. For more information concerning these parameters, the reader is referred to [14] and [35]. Furthermore, the required initial field for (3) is extracted from the ALADIN-CZ 6 h forecast data (see Table I) at 00h:00m and 12h:00m [38], [39].

The STD can be computed using [40]

$$\begin{aligned} \text{STD}(\text{ele}, \text{azi}) = & \text{ZHD} \cdot m f_h(\text{ele}) + \text{ZWD} \cdot m f_w(\text{ele}) \\ & + m f_g(\text{ele}) \cdot (G_N \cdot \cos(\text{azi}) \\ & + G_E \cdot \sin(\text{azi})) \end{aligned} \quad (4)$$

where ele and azi are the elevation angle and azimuth angle of the signal (in our processing, the minimum elevation cut-off angle is set to 5 degrees), ZHD and ZWD are the dry and wet delays in the zenith direction, respectively, and $m f_h$ and $m f_w$ are the dry and wet mapping functions, correspondingly [41]–[43]. G_N and G_E are the north-south and east-west components of the gradient delays. The required atmospheric pressure to derive ZHD has been derived from the mesoscale ALADIN-CZ 6 h forecast data and interpolated spatially to each GNSS reference station [18], [38]. Moreover, $m f_g$ is a gradient mapping function and computed as follows [44]:

$$m f_g(\text{ele}) = 1 / ((\sin(\text{ele}) \cdot \tan(\text{ele})) + 0.0032) \quad (5)$$

Therefore, the observation vector elements (SWD) can be obtained using (4) by subtracting the dry part from STD. For

this purpose, ZTD and the gradient delays are estimated using Bernese GNSS software [45]. Then, the dry part is removed by introducing the hydrostatic formulation [46] mapped with $m f_h$ (3). Finally, the remaining part is denoted as the Slant Wet Delay (SWD), although it also contains contributions caused by mismodeling of the hydrostatic component.

B. Straight-Line Geometry

To model the signal paths on their way between satellites and the receiver using straight-line geometry, the Cartesian Earth Fixed coordinates of all the satellites (from SP3 or the navigation file) and all receivers were transformed into the local NEU-system (North East Up) or in UTM (Universal Transverse Mercator) coordinates [47]–[49]. Then the line equation between satellite and GNSS station is calculated in the NEU or UTM Cartesian coordinate system based on the satellite coordinates and GNSS station coordinates. In addition, the tomography model is described as a set of planes in North-South, East-West, and Up direction. Therefore, each plane is defined by an analytic equation. For each GNSS line-of-sight equation, there is an intersection point with each of the planes in the model. Finally, the distance d_{mn} between inside pierce points is calculated to populate the design matrix $\mathbf{A}(2)$. The definition of the NEU and UTM coordinate systems is different in terms of accounting for Earth curvature and projection distortions. Therefore, the location of intersection points and, subsequently, the distance d_{mn} in the model elements are quite different, especially because our area of investigation is quite large (of about $250 \times 320 \times 10$ km).

C. Eikonal Ray-Tracing Method

According to (2), the ray length in each voxel should be computed using the ray-tracing method, which is one of the most important parts of tomography modeling. Consequently, we should use an accurate method, especially for low-elevation angles. One way to model the propagation of electromagnetic waves is Eikonal ray-tracing, which provides the ray path between receiver and satellite. (5) characterizes a partial differential of $N(\mathbf{r})$. It can be defined using Maxwell's equation as follows [50], [51]:

$$\|\Delta L\|^2 N(\mathbf{r})^2 \quad (6)$$

where L and ∇L are the optical path length and the components of ray directions, respectively. N is a refractive index and \mathbf{r} is a position vector. The Hamiltonian conical formalism is an important form for defining (5). The full derivation of the 3-D ray-tracer and its simplification to a 2-D case, under special conditions, is presented in Appendix A. Generally, any coordinate system can be chosen for solving (5). Nonetheless, according to Alkhalifah and Fomel [52], the spherical coordinate system is more accurate than the Cartesian coordinate system, as this is the most natural orthogonal system to solve the Eikonal equation in the case of a point source. In addition, this coordinate system usually meets the requirements of the ray tracing in the atmosphere. Therefore, the spherical coordinate system (φ, λ, h) is considered here to solve the Eikonal ray-tracer [29]. To investigate the impact of

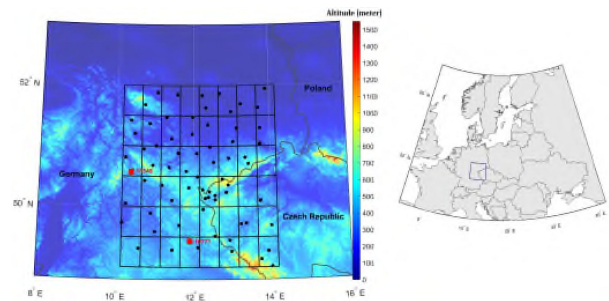


Fig. 1. Tomography model outline overlaid on topography and the administrative borders of central European countries. The GNSS network is marked with black points, and the red points represent the RS stations.

this coordinate system on the tomography results, the Eikonal raytracing equation is solved with neglecting the bending effect ($N = 1$).

According to Hobiger *et al.* [28], the ray-tracing outputs of the 2-D mode provide approximately the same results as the 3-D one, except for very-low-elevation angles. In addition, the computational efficiency of the 2-D ray-tracing method is preferable. Therefore, the 2-D Eikonal ray-tracing method is sufficient for our study. Finally, the distance d_{nm} between pierce points, which taking into account bending effects, is calculated to compute the design matrix elements (2).

D. Voxel Design Using Topography Effect

To apply a topography-in-tomography model, we should calculate the height of the grid point (φ, λ) according to the elevation model of the case study. Here, the shuttle radar topography mission (SRTM) image¹ has been used to count for the topography effect in the tomography model [53]. Several methods have been applied to find the highest precision for estimating the height of grid points in the tomography model. Linear interpolation, nearest neighbor interpolation, and Biharmonic spline interpolation are some of those methods. According to the obtained results, the nearest neighbor interpolation method was the best one for our case study. With this method, the quality of height interpolation of the grid point is better than 1 meter if the grid resolution is about $\pm 0.0083^\circ$ in the area of interest.

III. STUDY AREA

The area of interest ranges from 10.15° to 14° in longitude, 49° to 52° in latitude, and 0–15 km in WGS84 ellipsoidal height located in the central part of Europe. For more information please refer to [54]. Spatial distribution of GNSS stations and the first layer of the designed tomography model for this study is shown in Fig. 1. The GNSS network contains 72 stations, which are located mostly in western parts of the Czech Republic and East Germany. The maximum height difference between these stations is about 815 m.

Because of the atmospheric process that caused the central European floods in June 2013 [38], [55], Days of Year (DoYs) 160–176 (9–25 Jun) of that year were selected as the period

¹[Online]. Available: <http://srtm.csi.cgiar.org>

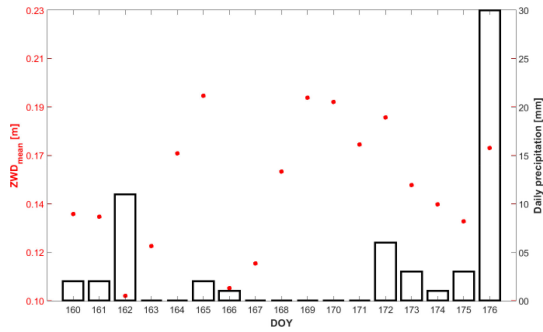


Fig. 2. Mean ZWD during the time of interest (red dots) plotted over daily precipitation (black bars) during the time of interest at Prague synoptic station [38].

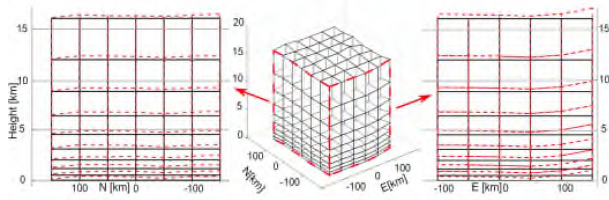


Fig. 3. Designed tomography model without topography (black solid lines) and with topography (red dashed lines). Left cross-section along S-N line and right cross-section along E-W line.

of interest (see Fig. 2). Fig. 2 shows the mean ZWD variation over the investigated period and the associated accumulated rain for Prague synoptic station. This period covers highly dynamic weather.

In addition, Table I shows an applied data set in the area of interest for tomography modeling.

According to previous research [18], the horizontal resolution of the tomographic model is 50 km with an exponential model in the vertical direction [20], [56], [57]. Moreover, a time resolution of 1 hour was applied for this research.

IV. NUMERICAL RESULTS

To analyze the effect of the topography in the area of tomographic modeling, we used two different schemes. In the first scheme, the tomography model was designed without topography information of the study region (Fig. 3: black lines on the left and right panel). In the second scheme, we designed the tomography model by considering topography information of the study area (Fig. 3: Red dashed lines in the left and right panels).

The clear difference between the two models is depicted in Fig. 3. It influences the design matrix A (2), as the location of intersection points between signal and model faces are shifted. Therefore, it changes the distance that each signal traveled through the tomography model (1). As seen in Fig. 3., the difference between using topography (red) and not using topography (black), especially in the North-East part, reaches up to 800 m, which corresponds to two layers at the bottom part of the model.

The consequence of the topography is visible also in Fig. 4, which shows that the number of rays passing through voxels in

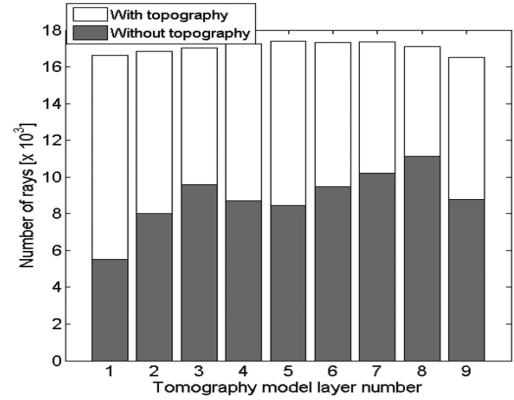


Fig. 4. Number of rays in each model layer (1 = bottom, 9 = top) within 1 hour (30 s observation update rate).

scheme 2 (with topography) is more than in scheme 1 (without topography).

Fig. 4 depicts a snapshot of one hour (23.30h–00.30h each investigated day). In general, the lowest layer is most affected, but satellite geometry can also cause a reasonable gain of intersected voxels in the upper layers. Therefore, when the topography effect is accounted for, we can expect an increased number of d_{nm} elements in the matrix A (2). In fact, increasing the redundancy of observations in each voxel can lead to a better reconstruction of the parameter of interest (due to lower condition number) in the desired voxel.

The essential increase of rays in the topography scheme is caused by additional rays originating from GNSS stations outside the tomography volume. This affects especially voxels located in columns close to the borders of the tomography volume.

Reference radiosonde observations were used to evaluate the effects of the topography and the different ray-tracing methods on the accuracy of the reconstructed field. For this purpose, we verified the estimated wet refractivity profile at Meiningen (RS10548) and Kammersbruk (RS10771) radiosonde stations (red dots in Fig. 1.) against the corresponding wet refractivity profile derived from the radiosonde observations at hours 00:00 and 12:00 UTC each day. Therefore, we have four reference profiles for each day. The height differences of Voxels in the location of radiosondes are about 318 and 360 m for RS10548 and RS10771, respectively.

To compare radiosonde and tomography profiles, all nine vertical layers from the reconstructed wet refractivity are considered. Moreover, the RS position is assumed to be in the same location at the center of Voxels. Then, the reconstructed field is interpolated using Inverse distance weighting on the RS location in each layer. Fig. 5 shows the agreement between the radiosonde profile and tomography wet refractivity for one selected epoch overall profile. In this figure, the model using topography is marked with red and the model without topography is marked with black. Each panel represents one processing approach: Fig. 5(a) Eikonal (see Section II, paragraph C); Fig. 5(b) Eikonal ($N = 1$); Fig. 5(c) straight line with topocentric coordinates (see Section II-B); Fig. 5(d) straight line with UTM projection (see Section II-B).

TABLE II
RMSE [MM/KM] OF WET REFRACTIVITY PROFILE FOR DIFFERENT SCHEMES FOR ALL DAYS AT EPOCH (00H: 00M IN UTC) FOR RS10548, BLACK BOXES MARK THE RAINY DAYS AND THE RED BOX MARKS THE WORST EPOCH SHOWN IN FIG. 5.

DoY	Eikonal +Topo	Eikonal (N=1) + Topo	Straight line [UTM+Topo]	Straight line [NEU+Topo]	Eikonal	Eikonal (N=1)	Straight line [UTM]	Straight line [NEU]
160	1.380	2.018	2.172	2.628	1.990	2.354	2.741	3.271
161	0.993	1.922	2.088	3.216	1.433	2.363	3.093	4.616
162	0.837	1.893	2.287	2.686	1.498	2.371	2.986	3.109
163	1.570	2.089	2.128	2.690	2.064	2.419	2.842	3.728
164	2.563	2.865	3.293	3.064	2.906	3.177	3.960	4.025
165	0.754	1.275	1.197	1.650	1.014	2.034	2.466	2.819
166	1.167	1.251	1.217	1.679	1.197	1.801	2.657	2.590
167	2.076	2.204	2.405	2.746	2.263	2.973	2.976	3.979
168	1.641	1.898	2.482	2.846	2.152	2.305	3.025	3.856
169	1.009	1.968	2.763	3.471	2.124	2.646	3.566	4.168
170	2.391	2.919	2.921	3.286	2.873	3.127	3.225	4.055
171	1.491	1.942	2.100	2.250	1.945	2.211	2.656	2.995
172	1.009	1.432	1.322	1.399	1.243	1.836	2.431	2.659
173	0.885	1.212	1.224	1.398	1.173	1.618	2.634	2.789
174	0.925	1.635	1.867	2.189	1.695	2.073	2.560	2.995
175	0.839	1.372	1.380	1.872	1.060	1.568	1.699	2.341
176	0.798	1.309	1.531	1.914	1.384	1.804	1.786	2.951
MEAN [mm/km]	1.313	1.836	2.022	2.411	1.766	2.275	2.783	3.350

TABLE III
RELATIVE ERROR REGARDING THE ALTITUDE OF THE LAYERS BELOW AND ABOVE 3 KM FOR THE FOUR TYPES OF PARAMETERIZATION, EIKONAL, EIKONAL (N = 1), NEU, AND UTM (BY CONSIDERING TOPOGRAPHY INFORMATION AND WITHOUT THAT) AT HOUR 00H:00M UTC FOR RS10548

Height	Eikonal +Topo	Eikonal (N=1) + Topo	Straight line [UTM+Topo]	Straight line [NEU+Topo]	Eikonal	Eikonal (N=1)	Straight line [UTM]	Straight line [NEU]
H≤3 km	0.044	0.073	0.076	0.093	0.071	0.091	0.104	0.138
H>3 km	0.295	0.308	0.372	0.617	0.367	0.316	1.986	1.072

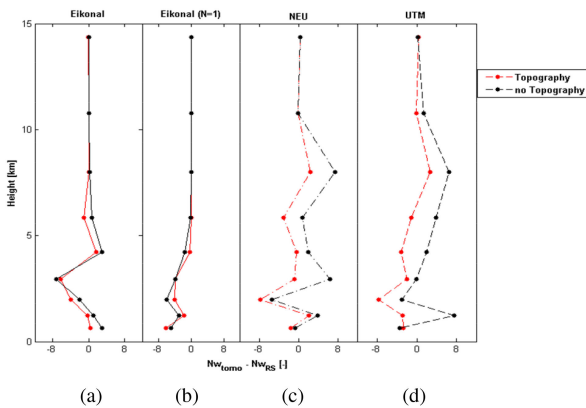


Fig. 5. Comparison of tomographic refractivity profiles (Nw_{tomo}) of different schemes to the profile derived from radiosonde data (Nw_{base}) DoY 164, at first epoch (00h:00m in UTC), for four types of parameterization, Eikonal, Eikonal ($N = 1$), NEU, and UTM by considering topography information and without topography.

The overall RMSE for all days considered for station Meiningen (RS10548) at 00h:00m in UTC (DoY 160 to DoY 176) is summarized in Table II. Results for the same station at 12h:00m

UTC and station Kummersbruk (RS10771) for both midnight and noon are presented in Appendix B.

Clearly, the best-performing algorithm is based on the Eikonal model with topography information included. The overall RMSE for all selected dates is 1.3 [mm/km], which is an improvement over the straight-line approach using UTM projection by 50%. The topocentric solution produces results with errors twice higher than the Eikonal with topography one which is 2.4 [mm/km]. A similar relation holds for the models without topography. The Eikonal solution is almost two times more accurate than the solution based on a straight line geometry (1.8 [mm/km] versus 3.4 [mm/km]). It is also worth mentioning that using topography improves the Eikonal solution by 34%. A similar improvement is visible for other parametrizations (NEU and UTM). Moreover, by ignoring the bending effect in (5) ($N = 1$), the impact of the spherical coordinate system in tomography solution is visible. According to these results, defining the coordinate system has considerable effect in the reconstructed field, especially when considering large areas with some hundred quadratic kilometers.

Further investigations focus on the selected case with the lowest accuracy in the set. For this case (DoY 164 00h:00m

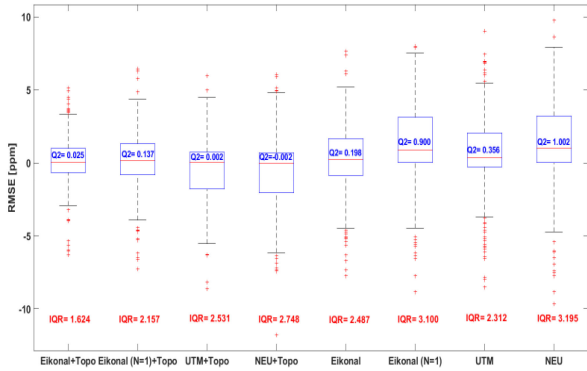


Fig. 6. Box plots of differences between the four types of parameterization, Eikonal, Eikonal ($N = 1$), NEU, and UTM (by considering topography information and without that) and RS10548 at hour 00h:00m and hour 12h:00m.

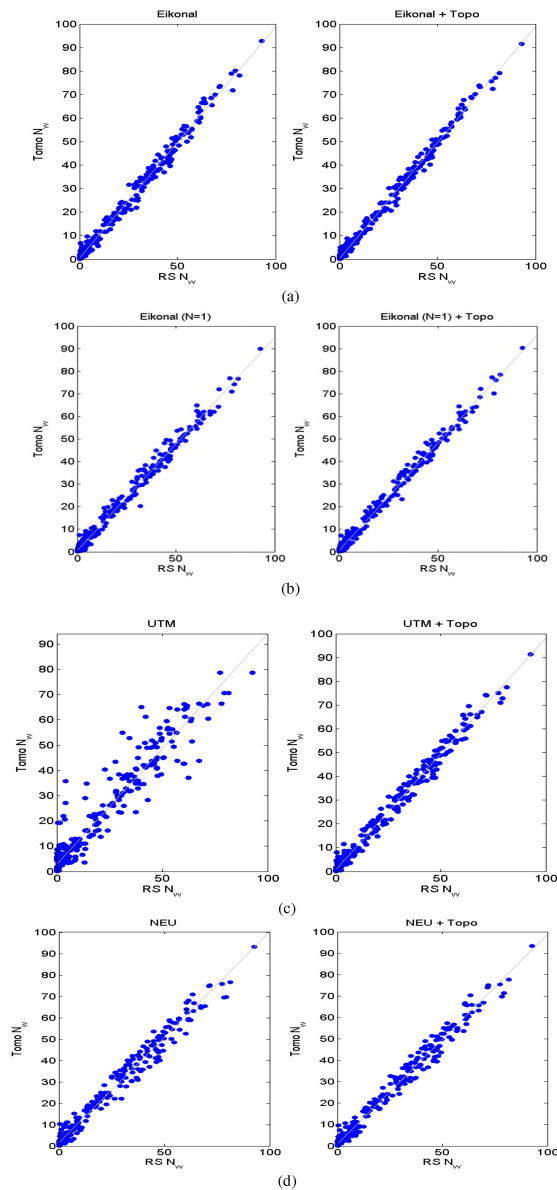


Fig. 7. Scatter plots of four types of parameterization, Eikonal, Eikonal ($N = 1$), NEU, and UTM by considering topography information and without that at hour 00h:00m and 12h:00m in year 2013 for RS10548.

UTC), clearly using topography in the most precise approach [see Fig. 5(a)] is required as the model without topography is producing biased fields (up to -7 mm/km) below 8 km. The impact of topography on the straight geometry [Eikonal ($N = 1$), NEU and UTM] is less definitive; however, Fig. 5(b) and (c) show a positive impact of topography for the middle levels (2–8 km).

To investigate the inconsistency between various parameterization methods with respect to the height, the relative error was applied [58]. According to Table III the height of 3 km, the relative errors of the Eikonal ray-tracing method with considering topography are superior to the other parameterization methods. Nevertheless, using this parameterization method in the upper layers does not have any considerable effect comparing to Eikonal ($N = 1$). In addition, applying topography in tomography modeling provides more reasonable reconstructed wet refractivity fields both in the upper and lower layers.

The statistical characteristics of the differences between the eight schemes and the radiosonde data are also presented by Fig. 6. Regarding the obtained box plots, the number of outliers in the Eikonal ray-tracing method is smaller than for other schemes. In this figure, IQR is defined as the difference between the first and third quartiles ($|Q1 - Q3|$) and shows the spread of data without outliers affect. Moreover, $Q2$ approximately represents the bias of all errors. Therefore, according to the obtained IQR and $Q2$ in Fig. 6, it can be concluded that Eikonal + Topo scheme is more concentrated and the NEU scheme shows an increased dispersion compared to other schemes.

Interestingly, Fig. 7 shows the dispersion of the reconstructed field (Tomo N_w) relative to the radiosonde profile (RS N_w) in different schemes at hour 00h:00m and hour 12h:00m in the time of interest. As shown in this figure, it is clear that the reconstructed wet refractivity field by Eikonal + Topo is more concentrated than other parameterization methods.

V. CONCLUSION

In this article, the effect of straight-line methods versus ray tracing methods was investigated for computing the length of a ray within a model element. This is a first attempt to reconstruct the wet refractivity field using the 2-D Eikonal raytracing method, which is a balance between the accuracy of 3D Eikonal raytracing and simplicity and processing speed of straight-line. Moreover, the accuracy of the ray-tracing method when the bending effect is neglected was investigated. In addition, we analyzed the effect to account for the topography in the tomography model.

A GNSS network in part of central Europe, which is based on the European COST Action ES1206, was used in our study. The accuracy of the developed model was verified using radiosonde measurements in the COST benchmark dataset.

The results showed that defining topography in the tomography model had a considerable impact on the lower layers on the reconstructed wet refractivity field. Moreover, applying the Eikonal ray-tracing method led to an improved accuracy of the estimated wet refractivity field compared to straight-line schemes (up to 84%). In the shown test case, area of about

250 × 320 × 10 km, the straight-line strategy performs much better in a UTM coordinate system than in a NEU coordinate system. Nevertheless, further investigation encompassing areas different in size is encouraged to achieve the general interpretation in the studied parameterization method.

APPENDIX A

Eikonal Ray-Tracing

According to Born and Wolf [50], Cerveny [59], Nafisi *et al.* [30] and Nilsson *et al.* [51], the Eikonal equation is presented as

$$H(\mathbf{r}, \nabla L) \equiv \frac{1}{\alpha} \left\{ (\nabla L \cdot \nabla L)^{\frac{\alpha}{2}} - N(\mathbf{r})^\alpha \right\} = 0 \quad (\text{A.1})$$

$$\frac{d\mathbf{x}_i}{du} = \frac{\partial H}{\partial \nabla L_i} \quad (\text{A.2})$$

$$\frac{d\nabla L_i}{du} = -\frac{\partial H}{\partial \mathbf{r}_i} \quad (\text{A.3})$$

$$\frac{dL_i}{du} = \nabla L_i \cdot \frac{\partial H}{\partial \nabla L_i}. \quad (\text{A.4})$$

Here, $H(\mathbf{r}, \nabla L)$ is the Hamiltonian function and α is a scalar value, which determines the type of the parameter of interest like arc length along the ray [29], [30], [51]. We need the length of the ray, so by setting $\alpha = 1$, (A.1) can be rephrased as

$$H(r, \theta, \lambda, L_r, L_\theta, L_\lambda) \equiv \left(L_r^2 + \frac{1}{r^2} L_\theta^2 + \frac{1}{r^2 \sin^2 \theta} L_\lambda^2 \right)^{\frac{1}{2}} - N(r, \theta, \lambda, t) = 0 \quad (\text{A.5})$$

where r , $0 \leq \theta \leq \pi$, and $0 \leq \lambda \leq 2\pi$ are the radial distance, the co-latitude, and the longitude, respectively. The elements of the ray direction are $L_r = \partial L / \partial r$, $L_\theta = \partial L / \partial \theta$, and $L_\lambda = \partial L / \partial \lambda$ [30]. By substituting (A.5) into (A.2) and (A.3), the first six equations in a spherical coordinate system are provided as

$$\frac{dr}{ds} = \frac{1}{\omega} L_r \quad (\text{A.6})$$

$$\frac{d\theta}{ds} = \frac{1}{\omega} \frac{L_\theta}{r^2} \quad (\text{A.7})$$

$$\frac{d\lambda}{ds} = \frac{1}{\omega} \frac{L_\lambda}{r^2 \sin^2 \theta} \quad (\text{A.8})$$

$$\frac{dL_r}{ds} = \frac{\partial N(r, \theta, \lambda, t)}{\partial r} + \frac{1}{\omega r} \left[\frac{L_\theta^2}{r^2} + \frac{L_\lambda^2}{r^2 \sin^2 \theta} \right] \quad (\text{A.9})$$

$$\frac{dL_\theta}{ds} = \frac{\partial N(r, \theta, \lambda, t)}{\partial \theta} + \frac{1}{\omega} \frac{L_\lambda^2}{r^2 \sin^3 \theta} \quad (\text{A.10})$$

$$\frac{dL_\lambda}{ds} = \frac{\partial N(r, \theta, \lambda, t)}{\partial \lambda} \quad (\text{A.11})$$

where the auxiliary parameter ω is defined as follows [30]:

$$\omega = \left(L_r^2 + \frac{1}{r^2} L_\theta^2 + \frac{1}{r^2 \sin^2 \theta} L_\lambda^2 \right) = N(r, \theta, \lambda, t). \quad (\text{A.12})$$

The positions of all points along the ray trajectory can be determined by solving (A.6)–(A.11) simultaneously [29], [30]. Here, the Runge-Kutta method, which is a known and standard approach to solve these equations, has been applied [30].

To solve these six partial differential equations, the initial conditions are needed. For this purpose, the station position at the starting point can be used as the initial condition [30], [59]

$$r = r_0 \quad (\text{A.13})$$

$$\theta = \theta_0 \quad (\text{A.14})$$

$$\lambda = \lambda_0 \quad (\text{A.15})$$

$$L_{r_0} = N_0 \cos z_0 \quad (\text{A.16})$$

$$L_{\theta_0} = N_0 r_0 \sin z_0 \cos \alpha_0 \quad (\text{A.17})$$

$$L_{\lambda_0} = N_0 r_0 \sin z_0 \sin \alpha_0 \sin \theta_0 \quad (\text{A.18})$$

where, α_0 and z_0 are the initial geodetic azimuth and zenith angle.

By setting the horizontal gradient of refractivity ($\partial N(r, \theta, \lambda, t) / \partial \theta$ and $\partial N(r, \theta, \lambda, t) / \partial \lambda$) to zero, the 3-D ray-tracing system is converted to 2-D ray-tracing. In this case, we assume that the ray path is limited to the vertical plane with constant azimuth. Therefore, the six partial equations (A.6)–(A.11) are reduced to four equations as follows:

$$\frac{dr}{ds} = \frac{1}{\omega} L_r \quad (\text{A.19})$$

$$\frac{d\theta}{ds} = \frac{1}{\omega} \frac{L_\theta}{r^2} \quad (\text{A.20})$$

$$\frac{dL_r}{ds} = \frac{\partial N(r, \theta, \lambda, t)}{\partial r} + \frac{1}{\omega r} \left[\frac{L_\theta^2}{r^2} + \frac{L_\lambda^2}{r^2 \sin^2 \theta} \right] \quad (\text{A.21})$$

$$\frac{dL_\theta}{ds} = \frac{1}{\omega} \frac{L_\lambda^2}{r^2 \sin^3 \theta}. \quad (\text{A.22})$$

APPENDIX B

TABLE IV

RMSE [MM/KM] OF WET REFRACTIVITY PROFILE FOR DIFFERENT SCHEMES DURING THE TIME OF INTEREST AT EPOCH (12H:00M IN UTC) FOR RS10548

DoY	Eikonal +Topo	Eikonal (N=1) + Topo	Straight line [UTM +Topo]	Straight line [NEU+Topo]	Eikonal	Eikonal (N=1)	Straight line [UTM]	Straight line [NEU]
160	1.045	1.996	2.009	2.585	1.658	2.017	2.780	3.282
161	1.097	1.728	2.127	2.364	1.648	2.034	2.672	2.658
162	0.952	1.874	1.969	2.317	1.358	1.894	2.505	2.948
163	1.610	2.066	2.616	2.812	1.975	2.619	2.978	3.113
164	2.075	2.409	2.767	3.185	2.489	2.784	3.156	3.528
165	1.604	2.097	2.158	2.529	2.045	2.185	2.507	2.936
166	1.206	1.957	2.001	2.353	1.598	2.237	2.580	2.709
167	2.439	2.865	3.268	3.821	2.620	2.808	3.750	3.908
168	2.478	2.638	2.993	3.301	2.868	3.254	3.442	3.595
169	2.796	3.140	3.292	3.750	3.196	3.433	3.778	3.999
170	2.697	2.885	3.504	3.643	3.177	3.578	3.834	4.109
171	1.924	2.302	2.749	3.135	2.219	2.886	3.020	3.467
172	1.674	1.984	2.065	2.108	1.826	2.011	2.149	2.308
173	1.096	1.731	1.916	2.291	1.483	2.219	2.440	2.664
174	2.540	2.957	3.943	4.646	3.137	3.984	4.385	4.996
175	1.971	2.512	2.550	2.769	2.305	2.504	2.724	3.008
176	1.765	2.004	2.096	2.101	2.089	2.186	2.303	2.527
MEAN [mm/km]	1.822	2.302	2.589	2.924	2.217	2.626	3.000	3.279

TABLE V
RMSE [MM/KM] OF WET REFRACTIVITY PROFILE FOR DIFFERENT SCHEMES DURING THE TIME OF INTEREST AT EPOCH (00H:00M IN UTC) FOR RS10771

DoY	Eikonal +Topo	Eikonal (N=1) + Topo	Straight line [UTM +Topo]	Straight line [NEU+ Topo]	Eikonal	Eikonal (N=1)	Straight line [UTM]	Straight line [NEU]
160	1.722	1.822	2.232	2.435	2.080	2.380	2.712	2.939
161	1.960	2.413	2.599	2.990	2.333	2.816	3.039	3.272
162	1.148	1.696	1.934	2.222	1.685	1.852	2.355	2.858
163	2.539	2.812	3.186	3.200	2.975	3.090	3.363	3.696
164	2.131	2.839	3.222	3.595	2.586	2.928	3.672	3.904
165	1.439	2.007	2.093	2.648	1.700	2.193	2.892	2.920
166	2.307	2.692	3.180	3.240	2.518	2.812	3.743	3.887
167	2.378	2.847	3.691	3.990	2.767	2.974	3.809	4.321
168	2.366	2.646	3.307	3.544	2.679	2.902	3.539	3.845
169	2.578	2.828	3.016	3.108	2.973	3.073	3.328	3.659
170	1.442	2.002	2.122	2.459	1.864	2.307	2.658	2.744
171	2.464	2.763	3.194	3.659	2.976	3.468	3.520	4.503
172	1.138	1.950	1.996	2.037	1.803	2.132	2.189	2.604
173	1.417	1.765	1.824	1.953	1.693	2.011	2.417	2.562
174	1.481	1.820	1.959	2.153	1.715	2.104	2.233	2.567
175	1.273	1.726	1.803	1.903	1.757	2.079	2.224	2.321
176	1.333	1.688	1.933	2.131	1.798	1.822	2.374	2.548
MEAN [mm/km]	1.830	2.254	2.546	2.780	2.229	2.526	2.945	3.244

TABLE VI
RMSE [MM/KM] OF WET REFRACTIVITY PROFILE FOR DIFFERENT SCHEMES DURING THE TIME OF INTEREST AT EPOCH (12H:00M IN UTC) FOR RS10771

DoY	Eikonal +Topo	Eikonal (N=1) + Topo	Straight line [UTM +Topo]	Straight line [NEU +Topo]	Eikonal	Eikonal (N=1)	Straight line [UTM]	Straight line [NEU]
160	1.504	1.819	2.031	2.517	1.962	2.282	2.410	2.969
161	1.410	1.598	2.121	2.227	1.975	2.212	2.670	2.808
162	1.590	1.801	1.960	2.163	1.790	2.136	2.522	2.671
163	1.985	2.360	2.497	2.814	2.313	2.524	2.729	3.056
164	1.985	2.467	2.760	3.134	2.561	3.158	3.343	3.525
165	1.299	2.260	2.505	2.691	1.956	2.553	2.774	2.995
166	2.596	2.740	3.062	3.567	2.951	3.017	3.756	3.888
167	2.680	3.066	3.427	3.694	3.226	3.408	4.292	4.504
168	2.874	3.217	3.495	3.853	3.472	3.625	3.922	4.339
169	1.645	1.942	2.266	2.531	2.146	2.333	2.569	2.904
170	2.102	2.413	2.740	2.882	2.663	2.887	3.026	3.206
171	2.913	3.438	3.864	3.987	3.562	3.823	4.149	4.223
172	1.648	1.908	2.004	2.145	1.723	1.946	2.374	2.576
173	1.787	2.255	2.340	2.522	2.280	2.970	3.003	3.095
174	2.015	2.664	2.706	3.323	2.639	2.826	3.031	3.700
175	1.561	2.035	2.416	2.495	2.061	2.697	2.717	2.773
176	2.264	2.680	2.927	2.953	2.754	2.972	3.445	3.773
MEAN [mm/km]	1.992	2.392	2.654	2.912	2.473	2.786	3.102	3.353

ACKNOWLEDGMENT

The authors would like to thank all the institutions and organizations that provided data for the COST Action ES1206 (GNSS4SWEC) to carry out this study. They also thank the SRTM site for providing the DEM model for our area of interest. They were also very thankful to the anonymous reviewers for

their valuable comments. This research was supported by "Interdisciplinary International Cooperation as the key to excellence in science and education (INCREaSE)" project.

REFERENCES

- [1] M. Troller, "GPS based determination of the integrated and spatially distributed water vapor in the troposphere," Ph.D. dissertation, ETH Zurich, Zurich, Switzerland, 2004.
- [2] Y. Yao, Q. Z. Zhao, and B. Zhang, "A method to improve the utilization of GNSS observation for water vapor tomography," *Ann. Geophys.*, vol. 34, pp. 143–152, 2016.
- [3] H. Brenot *et al.*, "A GPS network for tropospheric tomography in the framework of the Mediterranean hydrometeorological observatory Cévennes-Vivarais (southeastern France)," *Atmos. Meas. Techn.*, vol. 7, pp. 553–578, 2014.
- [4] S. M. Lutz, "High-resolution GPS tomography in view of hydrological hazard assessment," Ph.D. dissertation, ETH Zurich, Zurich, Switzerland, 2008.
- [5] T. Manning, K. Zhang, W. Rohm, S. Choy, and F. Hurter, "Detecting Severe Weather using GPS tomography: An Australian case study," *J. Global Positioning Syst.*, vol. 11, pp. 58–70, 2012.
- [6] D. C. Norquist and S. S. Chang, "Diagnosis and correction of systematic humidity error in a global numerical weather prediction model," *Monthly Weather Rev.*, vol. 122, pp. 2442–2460, 1994.
- [7] J. Zhang, "Investigations into the Estimation of Residual Tropospheric Delays in a GPS Network," M.Sc. Dept. Geomatics Eng., Calgary, AB, Canada, Art. no. 20132, 1999.
- [8] O. Bock, J. Tarniewicz, C. Thom, and J. Pelon, "Effect of small-scale atmospheric inhomogeneity on positioning accuracy with GPS," *Geophys. Res. Lett.*, vol. 28, no. 11, pp. 2289–2292, 2001.
- [9] J. Braun and C. Rocken, "Water vapor tomography within the planetary boundary layer using GPS," in *Proc. Int. Workshop GPS Meteorol.*, 2003, pp. 3-09–1-4.
- [10] J. Tarniewicz, O. Bock, J. Pelon, and C. Thom, "Raman lidar for external GPS path delay calibration devoted to high accuracy height determination," *Phys. Chem. Earth, Parts A/B/C*, vol. 27, no. 4, pp. 329–333, 2002.
- [11] J. Braun, C. Rocken, and J. Liljegren, "Comparisons of line-of-sight water vapor observations using the global positioning system and a pointing microwave radiometer," *J. Atmos. Ocean. Technol.*, vol. 20, no. 5, pp. 606–612, 2003.
- [12] A. H. Dodson, P. J. Shardlow, L. C. M. Hubbard, G. Elgered, and P. O. J. Jarlemark, "Wet tropospheric effects on precise relative GPS height determination," *J. Geodesy*, vol. 70, no. 4, pp. 188–202, 1996.
- [13] P. M. Herschke, "Modeling and extrapolation of path delays in GPS signals," Master thesis ETH Zurich, Zürich, Switzerland, 2002.
- [14] Z. Adavi and M. Mashhadi Hossainali, "4D-Tomographic reconstruction of the tropospheric wet refractivity using the concept of virtual reference station, case study: North west of Iran," *Meteorol. Atmos. Phys.*, vol. 125, no. 3–4, pp. 193–205, 2014.
- [15] M. Bender *et al.*, "Development of a GNSS water vapour tomography system using algebraic reconstruction techniques," *Adv. Space Res.*, vol. 47, pp. 1704–1720, 2011.
- [16] H. Brenot *et al.*, "Cross-Comparison and methodological improvement in GPS tomography," *Remote Sens.*, vol. 12, no. 30, 2020.
- [17] A. Flores, "Atmospheric tomography using satellite radio signals," Ph.D. dissertation, de Teoria del Senyal i Comunicacions, Politècnica de Catalunya, Barcelona, Spain, 1999.
- [18] N. Hanna, E. Trzcina, G. Möller, W. Rohm, and R. Weber, "Assimilation of GNSS tomography products into WRF using radio occultation data assimilation operator," *Atmos. Meas. Tech. Discuss.*, vol. 2019, pp. 1–32, 2019.
- [19] S. M. Lutz, "High-resolution GPS tomography in view of hydrological hazard assessment," Geodätisch-geophysikalische Arbeiten in der Schweiz, Swiss Geodetic Commission, vol. 76, 2009.
- [20] T. Manning, "Sensing the dynamics of severe weather using 4D GPS tomography in the Australian region," Ph.D. dissertation, School of Mathematical and Geospatial Sci. College Sci., Engineering, and Health, Royal Melbourne Inst. Technol. Univ., Melbourne, VIC, Australia, 2013.
- [21] T. Nilsson, L. Gradinarsky, and G. Elgered, "GPS tomography using phase observations," in *Proc. Geosci. Remote Sens. Symp.*, 2004, pp. 2756–2759.
- [22] D. Perler, A. Geiger, and F. Hurter, "4D GPS water vapor tomography: New parameterized approaches," *J. Geodesy*, vol. 85, pp. 539–550, 2011.

- [23] W. Rohm and J. Bosy, "Local tomography troposphere model over mountains area," *Atmos. Res.*, vol. 93, no. 4, pp. 777–783, 2009.
- [24] W. Rohm, K. Zhang, and J. Bosy, "Limited constraint, robust Kalman filtering for GNSS troposphere tomography," *Atmos. Meas. Techn.*, vol. 7, pp. 1475–1486, 2014.
- [25] E. Trzcina and W. Rohm, "Estimation of 3D wet refractivity by tomography, combining GNSS and NWP data: First results from assimilation of wet refractivity into NWP," *Quar. J. Roy. Meteorol. Soc.*, vol. 145, no. 720, pp. 1034–1051, 2019.
- [26] Y. Yao and Q. Zhao, "A novel, optimized approach of voxel division for water vapor tomography," *Meteorol. Atmos. Phys.*, vol. 129, pp. 57–70, 2017, doi: [10.1007/s00703-016-0450-4](https://doi.org/10.1007/s00703-016-0450-4).
- [27] G. Möller and D. Landskron, "Atmospheric bending effects in GNSS tomography," *Atmos. Meas. Tech.*, vol. 12, no. 1, pp. 23–34, 2019.
- [28] T. Hobiger, R. Ichikawa, Y. Koyama, and T. Kondo, "Fast and accurate ray-tracing algorithms for real-time space geodetic applications using numerical weather models," *J. Geophys. Res., Atmos.*, vol. 113, no. D20, pp. 1–14, 2008.
- [29] A. Hofmeister, "Determination of path delays in the atmosphere for geodetic VLBI by means of ray-tracing," Ph.D. dissertation, Dept. Geodesy Geophys., Faculty of Math. Geoinf., Technische Universität Wien, Vienna, Austria, 2016.
- [30] V. Nafisi, M. Madzak, J. Böhm, A. A. Ardalan, and H. Schuh, "Ray-traced tropospheric delays in VLBI analysis," *Radio Sci.*, vol. 47, no. 2, pp. 1–17, 2012.
- [31] S. Haji Aghajany and Y. Amerian, "Three dimensional ray tracing technique for tropospheric water vapor tomography using GPS measurements," *J. Atmos. Solar-Terrestrial Phys.*, vol. 164, pp. 81–88, 2017.
- [32] W. Menke, *Geophysical Data Analysis: Discrete Inverse Theory*, MATLAB Edition, 3rd ed. Cambridge, MA: Acad. Press, 2012, p. 330.
- [33] M. Bender *et al.*, "GNSS Water Vapor Tomography," in *Deutsches Geo-Forschungszentrum*. Postdam, Germany: GFZ, 2013.
- [34] C. Champollion *et al.*, "GPS water vapour tomography: Preliminary results from the ESCOMPTE field experiment," *Atmos. Res.*, vol. 74, pp. 253–274, 2005.
- [35] Z. Adavi and R. Weber, "Evaluation of virtual reference station constraints for GNSS tropospheric tomography in Austria region," *Adv. Geosci.*, vol. 50, pp. 39–48, 2019.
- [36] T. Elfving, T. Nikazad, and P. C. Hansen, "Semi-Convergence and relaxation parameters for a class of SIRT algorithms," *Electron. Trans. Numer. Anal.*, vol. 37, pp. 321–336, 2010.
- [37] P. C. Hansen, *Rank-Deficient and Discrete ILL-Posed Problems: Numerical Aspect of Linear Inversion*. Philadelphia, PA, USA: SIAM, 1998, p. 264.
- [38] J. Douša *et al.*, "Benchmark campaign and case study episode in central Europe for development and assessment of advanced GNSS tropospheric models and products," *Atmos. Meas. Tech.*, vol. 9, pp. 2989–3008, 2016.
- [39] A. Farda, M. Déué, S. Somot, A. Horányi, V. Spiridonov, and H. Tóth, "Model aladin as regional climate model for central and eastern Europe," *Studia Geophysica et Geodaetica*, vol. 54, no. 2, pp. 313–332, 2010.
- [40] M. Kačmarčík *et al.*, "Inter-technique validation of tropospheric slant total delays," *Atmos. Meas. Tech.*, vol. 10, no. 6, pp. 2183–2208, 2017.
- [41] J. Böhm, A. Niell, P. Tregoning, and H. Schuh, "Global Mapping Function (GMF): A new empirical mapping function based on numerical weather model data," *Geophys. Res. Lett.*, vol. 33, 2006, Art. no. L07304.
- [42] J. Böhm, B. Werl, and H. Schuh, "Troposphere mapping functions for GPS and VLBI from ECMWF operational analysis data," *Geophys. Res.*, vol. 111, pp. 1–9, 2006.
- [43] D. Landskron and J. J. o. G. Böhm, "VMF3/GPT3: Refined discrete and empirical troposphere mapping functions," *J. Geodesy*, vol. 92, no. 4, pp. 349–360, Apr. 01, 2018.
- [44] G. Chen and T. A. Herring, "Effects of atmospheric azimuthal asymmetry on the analysis of space geodetic data," *Geophys. Res.*, vol. 102, no. B9, pp. 20489–20502, 1997.
- [45] R. Dach, S. Lutz, P. Walser, and P. Fridez, *Bernese GNSS Software Version 5.2. Astronomical Institute*. Bern, Switzerland: Univ. Bern, 2015.
- [46] J. Saastamoinen, "Contributions to the theory of atmospheric refraction. Part II: Refraction corrections in satellite geodesy," *Bull. Géodésique*, vol. 107, pp. 13–34, 1973.
- [47] G. Cai, B. M. Chen, and T. H. Lee, *Unmanned Rotorcraft Systems*. Berlin, Germany: Springer, 2011.
- [48] M. S. Grewal, R. L. Weill, and A. P. Andrews, *Global Positioning Systems, Inertial Navigation, and Integration*. Hoboken, NJ, USA: Wiley, 2007.
- [49] M. R. Siegfried, "Inversion of extremely ill-conditioned matrices in floating-point," *Jpn. J. Ind. Appl. Math.*, vol. 26, no. 2, pp. 249–277, 2009.
- [50] M. Born and E. Wolf, *Principles of Optics*. New York, NY, USA: Cambridge Univ. Press, 1999.
- [51] T. Nilsson, J. Böhm, D. D. Wijaya, A. Tresch, V. Nafisi, and H. Schuh, "Path delays in the neutral atmosphere," in *Atmospheric Effects in Space Geodesy*. J. Böhm and H. Schuh, Eds. Berlin, Germany: Springer, 2013, pp. 73–136.
- [52] T. Alkhalifah and S. Fomel, "Implementing the fast marching Eikonal solver: Spherical versus Cartesian coordinates," *Geophys. Prospect.*, vol. 49, pp. 165–178, 2001.
- [53] B. Kaltenbacher, A. Neubauer, and O. Scherzer, *Iterative Regularization Methods for Nonlinear Ill-Posed Problems*. Berlin, Germany: De Gruyter, 2008.
- [54] F. B. Belgacem and S.-M. Kaber, "Ill-conditioning versus ill-posedness for the boundary controllability of the heat equation," *J. Inverse Ill-Posed Problems*, vol. 23, no. 4, 2013.
- [55] J. Böhm, B. Werl, and H. Schuh, "Troposphere mapping functions for GPS and very long baseline interferometry from European centre for medium-range weather forecasts operational analysis data," *J. Geophys. Res.*, vol. 111, 2006, Art. no. B02406.
- [56] G. Möller, "Reconstruction of 3D wet refractivity fields in the lower atmosphere along banded GNSS signal paths," Ph.D. dissertation, TU Wien, Dt. Geodesy Geoinf., 2017.
- [57] D. Perler, "Water vapour tomography using global navigation satellite systems," Ph.D. dissertation, ETH, Zurich, Switzerland, 2011.
- [58] Q. Zhao, K. Zhang, Y. Yao, and X. J. G. S. Li, "A new troposphere tomography algorithm with a truncation factor model (TFM) for GNSS networks," *GPS Solution*, vol. 23, no. 3, pp. 1–13, Apr. 17, 2019.
- [59] V. Cerveny, *Seismic Ray Theory*. Cambridge, U.K.: Cambridge Univ. Press, 2005, pp. 1–722.



Zohreh Adavi received the B.S. and M.S. degrees in geomatics engineering from the KNTU University of Technology, Tehran, Iran.

She is currently working as a Project Assistant with the Geodesy and Geoinformation Department, Vienna University of Technology. Her recent and current research interests include GNSS Tomography and parameter estimations of ill-conditioned problems.



Witold Rohm received both Doctoral and Habilitated doctor degrees at Wrocław University of Environmental and Life (UPWr), Wrocław, Poland, in 2011 and 2015, respectively.

He is an Associate Professor with UPWr. He has authored more than 40 journal papers and more than 20 conference papers. His current research interests include integration of tropospheric observations from different sources, assimilation of GNSS tomography outputs in weather models, and use of AI in remote sensing.



Robert Weber received the Ph.D. degree in geodesy and geoinformation and passed habilitation from Vienna University of Technology, in 1998.

He is an Associate Professor with Vienna University of Technology, Vienna, Austria. His main fields of research are global navigation satellite systems, geodetic reference systems, active GNSS reference station networks and applications of GNSS for geodynamics, and meteorology.

Dr. Weber was the recipient of the Austrian Hopfner Medal (2018).